Probing the Solar Magnetic Field with a Sun-Grazing Comet

Cooper Downs *et al.*

Science **340**, 1196 (2013);
DOI: 10.1126/science.1236550

Probing the Solar Magnetic Field with a Sun-Grazing Comet

Cooper Downs,[1]* Jon A. Linker,[1] Zoran Mikić,[1] Pete Riley,[1] Carolus J. Schrijver,[2] Pascal Saint-Hilaire[3]

On 15 and 16 December 2011, Sun-grazing comet C/2011 W3 (Lovejoy) passed deep within the solar corona, effectively probing a region that has never been visited by spacecraft. Imaged from multiple perspectives, extreme ultraviolet observations of Lovejoy's tail showed substantial changes in direction, intensity, magnitude, and persistence. To understand this unique signature, we combined a state-of-the-art magnetohydrodynamic model of the solar corona and a model for the motion of emitting cometary tail ions in an embedded plasma. The observed tail motions reveal the inhomogeneous magnetic field of the solar corona. We show how these motions constrain field and plasma properties along the trajectory, and how they can be used to meaningfully distinguish between two classes of magnetic field models.

The Sun's magnetic field is of primary importance in solar and heliospheric physics. It is the energy source for solar activity, and it defines the structure of the solar corona and of the solar wind, which is largely determined in the low solar corona (~1 to 2 solar radii, R_S, measured from Sun center). It is extremely difficult to measure the coronal magnetic field directly. Although our understanding of the corona has greatly improved with sophisticated remote sensing techniques and modeling methods, models and extrapolations explicitly depend on photospheric magnetic field observations (which provide only a partial constraint on the extended field) as a boundary condition. Because of the extremely harsh near-Sun environment, even the most advanced near-Sun exploration mission planned to date—Solar Probe Plus (*1*), which will take a spacecraft within 8.5 R_S of the solar surface—leaves a crucial measurement gap between the base of the solar atmosphere and the extended solar wind. It is for this reason that an opportunity to independently probe the plasma and magnetic state of the low corona is an important occurrence. In December 2011, one such opportunity came in the form of a naturally occurring celestial explorer: Sun-grazing Kreutz-family (*2*) comet C/2011 W3 (Lovejoy), the first Sun-grazer observed to survive its approach and reemerge from the corona (*3*), and the second comet observed within the corona at extreme ultraviolet (EUV) wavelengths (*4*).

With a perihelion of 1.2 R_S, comet Lovejoy came within 140,000 km of the visible solar surface. At heliocentric distances of 1.2 to 2.0 R_S, which are above the typical usable heights for stereoscopic or tomographic reconstructions of the coronal magnetic field and plasma state (*5*, *6*), this passage was imaged from multiple viewpoints by three space-based EUV-imaging telescopes: the Atmospheric Imaging Assembly (AIA) aboard the NASA Solar Dynamics Observatory and the Extreme Ultraviolet Imagers (EUVI-A and EUVI-B) aboard the twin NASA STEREO spacecraft, which were located ~107° ahead and behind Earth's orbit at this time. Base ratio 171 Å images of Lovejoy's tail evolution in the corona are shown

[1]Predictive Science Inc., 9990 Mesa Rim Road, Suite 170, San Diego, CA 92121, USA. [2]Lockheed Martin Advanced Technology Center, 3251 Hanover Street, Palo Alto, CA 94304, USA. [3]Space Sciences Laboratory, University of California, Berkeley, CA 94720, USA.

*Corresponding author. E-mail: cdowns@predsci.com

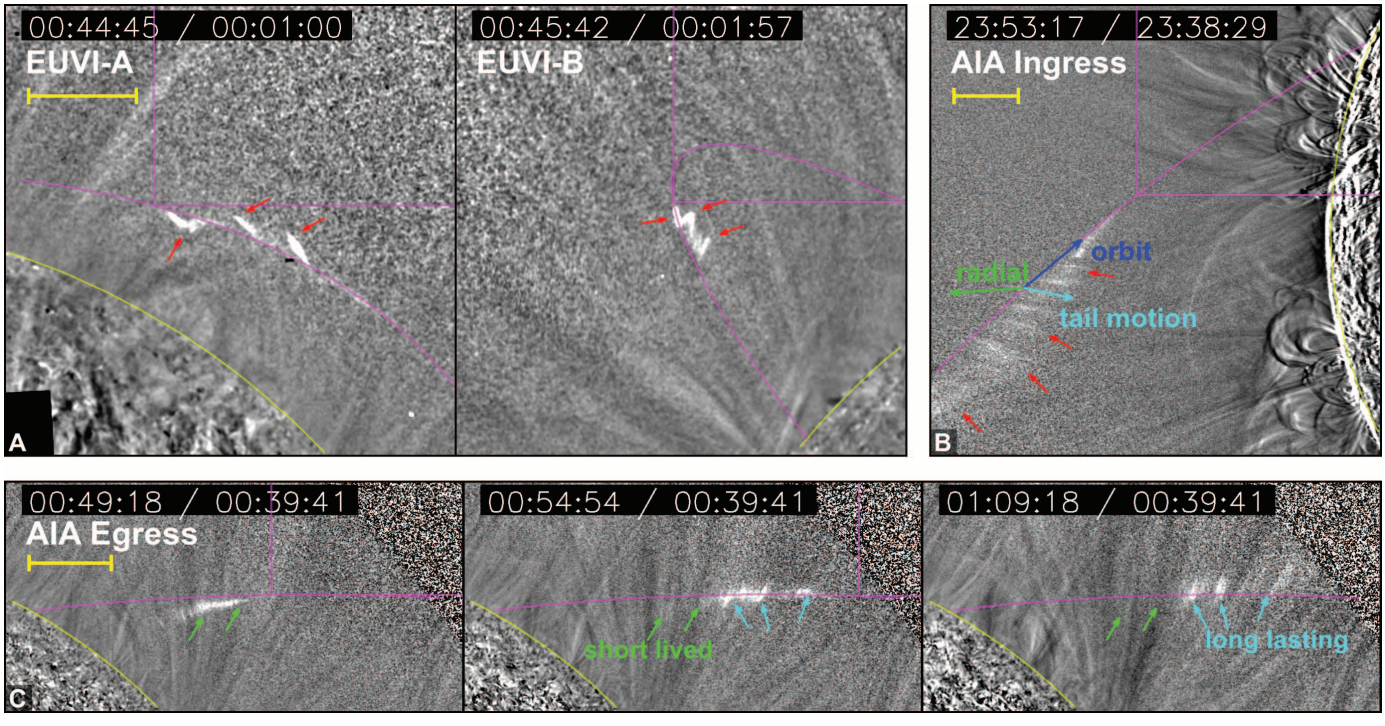

Fig. 1. Comet Lovejoy's tail dynamics in the corona. Base ratio processed 171 Å EUV observations from multiple viewpoints are shown; the white enhancements highlighted by short red arrows indicate the emitting comet tail. (**A**) EUVI-A and EUVI-B images that show the apparent "wiggles" out of the orbital path observed during the closest approach. (**B**) An AIA image before perihelion (ingress) with arrows indicating the southwest tail motion and other relevant directions. (**C**) The long-lasting portions of the tail are highlighted, with a time sequence of post-perihelion AIA images (egress) that show a separation of approximately 5.5 and 15.5 min, respectively. The yellow scale bar in each panel indicates a length of 100 Mm (10^5 km) in the plane of the sky (POS), the Sun-centered plane normal to the spacecraft. See movies S1 to S4 for the full observations for each view. Image timestamps are UT between 15 and 16 December 2011.

in Fig. 1. The apparent "wiggles" out of the orbital path observed by EUVI-A and EUVI-B (Fig. 1A) suggest a rapid change in the way in which comet tail ions are either channeled by or influence the ambient coronal medium. AIA observations before perihelion (ingress, Fig. 1B) show that the comet tail motion was markedly in the southwest direction. This motion corresponded neither to radial motion, which would be expected if the tail motion were dominated by solar wind outflows or radiation pressure, nor to motion tangential to the comet orbit, which would be expected if the medium had no influence at all. After perihelion (egress, Fig. 1C), observable tail emission nearer to the Sun (left half) had a relatively short lifetime ($\tau \leq 5$ min) while the portion located farther out remained much longer ($\tau \geq 15$ min). In some of these longer-lasting regions, the projected tail emission continued to evolve anisotropically, forming contrasted linear features not aligned with the orbital path (Fig. 1C, right). This behavior was also similarly observed during ingress.

A thorough description of how EUV emission can occur from cometary material injected into the corona was given by Bryans and Pesnell (*7*), who modeled the comet tail as a cylinder along the orbit path and used ion outflow velocities of 10 to 100 km s^{-1} as plausible limits on the overall width. Here, we additionally take into account the presence of the magnetic field in determining the geometrical shape and evolution of the tail. Consider the following chain of events for a cometary oxygen (O) test particle under "standard" coronal conditions ($r < 1.2\ R_S$, electron number density $n_e \sim 10^8$ cm^{-3}, electron temperature $T_e \sim 1.5$ MK): A molecule containing O that was originally part of the solid comet body (the largest contributor being water ice) is sublimated via insolation from the comet surface with some outflow velocity. This molecule will quickly be photodissociated ($\tau \sim 2.9$ s) and the free neutral O atom is rapidly ionized via charge exchange with coronal protons and collisions with coronal electrons ($\tau \leq 0.07$ s for $O \rightarrow O^+$).

In the inertial frame of the Sun, this ion will initially have the vector sum of the thermal, outflow, and comet velocities ($\mathbf{v}_i = \mathbf{v}_t + \mathbf{v}_{out} + \mathbf{v}_c$).

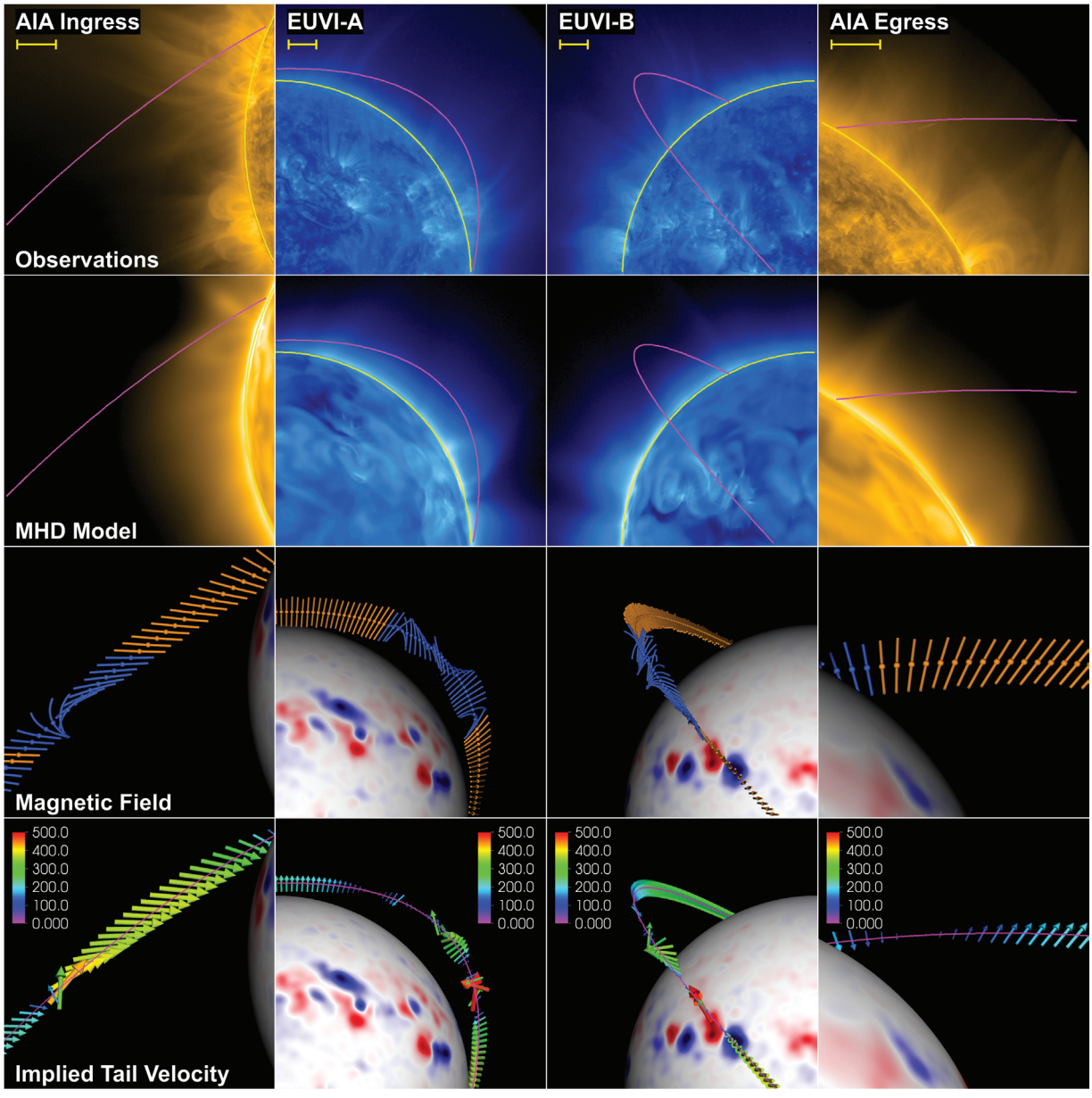

Fig. 2. Modeled coronal environment for each view of the comet flyby. The top two rows show a comparison between 171 Å imaging observations and synthesized emission from the model solution. The bottom rows show the local magnetic field along the comet trajectory (blue, closed field; orange, open field) and the implied initial tail velocity, $(\mathbf{v}_c \cdot \hat{b})\hat{b}$ (arrows). The relative size and color of the arrows is proportional to the magnitude of $(\mathbf{v}_c \cdot \hat{b})\hat{b}$ in km s^{-1}. As in Fig. 1, the yellow scale bars in the top row indicate a length of 100 Mm in the POS.

Assuming a locally fixed magnetic field, the newly felt Lorentz force will cause the ion to gyrate about the magnetic field, effectively eliminating perpendicular flow on a macroscopic scale while leaving the parallel component unmodified; that is, $\mathbf{v}_i \rightarrow \mathbf{v}_{i,macro} = (\mathbf{v}_i \cdot \hat{b})\hat{b} = v_p\hat{b}$, where v_p is the speed parallel to the field direction, $\hat{b} = \mathbf{B}/|\mathbf{B}|$. where $\mathbf{B}$ is the local magnetic field vector.

As the test particle flows along the given field line, it will decelerate and thermalize via collisional momentum/energy exchange with the ambient plasma (ions, protons, and electrons). As this occurs, electron impact ionization serves to successively raise the ionization state to states where EUV emission lines are visible in the AIA channels, such as O V, O VI, and Fe IX in the case of the 171 Å channel, which occurs at successively longer time scales. Because the "tail," as seen in the EUV, is simply a tracer for the location of emitting ions as they interact with the medium, the apparent motion of the tail can thus be approximated by considering the motion and subsequent deceleration of cometary ions flowing parallel to the coronal magnetic field (*8*).

This scenario opens up the possibility of testing one or more model coronae. Through their validation, we obtain information on the coronal field and on the plasma state along and around the comet's trajectory. To do so, we used a state-of-the-art three-dimensional (3D) thermodynamic magnetohydrodynamic (MHD) model of the global corona, tailored to best approximate the corona during perihelion (*9*). This massively parallel computation involved solving for the full 3D magnetic field and plasma state (flow, magnetic field, temperature, and density) in a global spherical domain from 1.0 to 20 R_S. We assessed the final thermodynamic state by comparing synthetic multiwavelength images generated from the solution directly to observational data (Fig. 2, top rows).

The local magnetic field along the comet trajectory gives a sense of the complex local magnetic geometry encountered by the comet, which

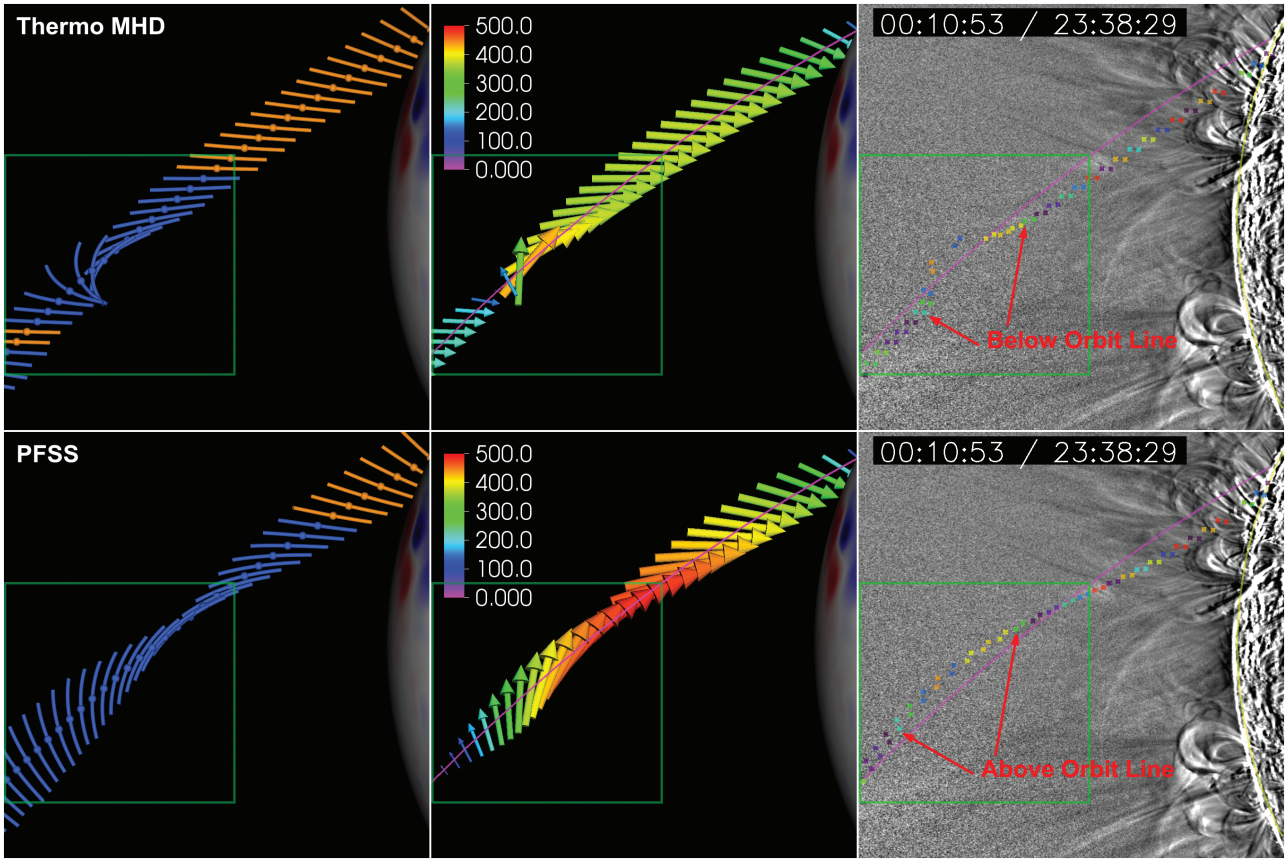

Fig. 3. Predicted tail motion for two magnetic field models. Comparison of the magnetic field (**left**), initial tail velocity $(\mathbf{v}_c \cdot \hat{b})\hat{b}$ (**center**), and resulting comet tail flow (**right**) predicted by the thermodynamic MHD model (top row) and the PFSS field model (bottom row) for the AIA ingress observations.

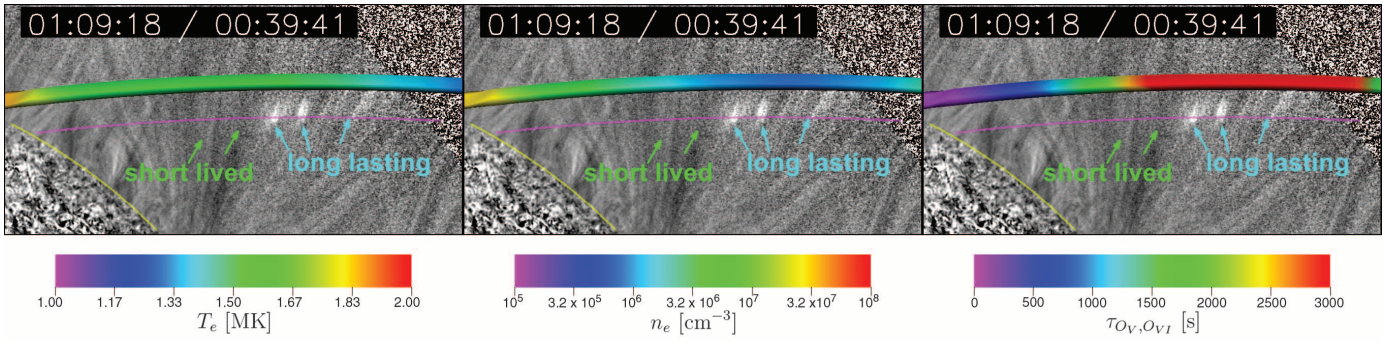

Fig. 4. Estimates of the tail lifetime from MHD model data. MHD model overlays of electron temperature (**left**), electron density (**center**), and the lifetime estimate, $\tau_{OV,OVI}$ (**right**), over the AIA egress observations. The MHD data along the trajectory are shown as a wide color contour placed above the orbit line.

is used to infer the initial direction and magnitude of comet tail ion velocity, $(\mathbf{v}_c \cdot \hat{b})\hat{b}$ (Fig. 2, bottom rows). Examining each view, we gain a sense for how the field orientation implies nonradial and nonorbital directions for tail motion, as well as rapid switching in some regions due to the changing 3D magnetic field structure. Note that the comet trajectory is interspersed with closed-field regions (blue lines) where the field orientation is changing rapidly in the comet frame, which similarly modifies $(\mathbf{v}_c \cdot \hat{b})\hat{b}$ over short time periods.

To fully link the MHD solution with the observations, we probed the comet tail evolution by approximating the deceleration of cometary ions along the magnetic field as an exponential decay with time constant τ_d = 150 s plus flow and diffusion terms. This reduced the comet tail dynamics to the ballistic tracking of test particles within a 3D vector field and inhomogeneous medium (*10*).

One obvious use of the tail model applied to 3D field distributions is the comparison of results between two distinct coronal field models. We illustrate this idea by comparing the field produced by the thermodynamic MHD solution to a potential field source surface (PFSS) calculation for the same boundary conditions. Originally described by Schatten *et al*. (*11*), the PFSS model has become a standard tool for rapid and reasonable estimates of coronal fields. Unlike the thermodynamic MHD calculation, the PFSS solution assumes that the domain is current-free at all heights up to a source surface radius where the field becomes radial (typically 2.5 R_S). However, PFSS solves only for the minimum energy state of the coronal field distribution, and therefore does not capture structures energized through sustained motions and thermodynamic forces.

There is an overall global resemblance between the thermodynamic MHD and PFSS solutions, which is not unexpected for regions with low relative electric currents (*12*). However, because this MHD model resolves thermodynamic forces that become non-negligible in regions where the magnetic field is weak relative to the plasma pressure, the details of the closed-field streamer regions, and hence the precise comet tail dynamics, are expected to differ. Comparing them in Fig. 3, we find that the thermodynamic MHD model captures the southwest direction of the tail during the initial ingress from 23:40 to 23:55 UT (green box). Because the curvature of the field on the east side of the streamer region (blue lines, lower left) differs between the two models, the comet flow prediction is in the opposite (northeast) direction for the PFSS model during this time period. This mismatch in tail motion may be due to missing forces in the PFSS model, although a PFSS model with a lower source surface might perform better. Neither the MHD model nor the PFSS model reproduced the southwestern motion between 23:45 and 23:48 UT, which passes through the cusp of the closed-field region. The exact location of this feature is more sensitive to model parameters as well as the boundary conditions, which lack the most recent photospheric observations on this side of the Sun (because of solar rotation). In any case, this comparison highlights the capability of the comet tail observations to corroborate or invalidate portions of global field models—an otherwise nontrivial task fraught with ambiguity.

We also considered the long-lasting portion of the comet tail in terms of the thermodynamic state along the trajectory in the MHD model (Fig. 4). A rough lifetime estimate for O^{4+} and O^{5+} ions, and hence their emission time scale in a coronal plasma, $\tau_{OV,OVI}$, can be calculated from the electron impact ionization rates under the assumption that they scale with the local electron density (*13*). Using the MHD model values to compute $\tau_{OV,OVI}$, we find that this time scale is considerably lengthened relative to "typical" ($n_e = 10^8$ cm^{-3}) coronal conditions for the later half of the view, which is qualitatively consistent with the transition from short to long lifetime in the tail observations (albeit broader and slightly offset). The longer time scales can also help to explain the relative constancy of emission from the long-lasting portions of the tail.

Extensions to the parallel flow model, such as the inclusion of perpendicular ion flow mechanisms, drifts, or coronal field modifications [e.g., (*14*)], could provide deep insight into the two-way coupling of the comet to the coronal field itself. Such a scenario is likely needed to explain the slow but conspicuous backward-projected motion of a portion of the tail around 00:01 UT during ingress (*9*). Looking forward, a higher frequency of such Sun-grazing comets is predicted for this decade (*3*, *15*), and another large comet is predicted to pass through the solar atmosphere in November 2013 [comet C/2012 S1 (ISON) (*16*)]. This bolsters the exciting prospect that coronal observations of comet flybys can offer a unique and complementary avenue toward understanding the solar atmosphere.

References and Notes

1. *Solar Probe Plus: Report of the Science and Technology Definition Team*, NASA/TM-2008-214161 (2008).
2. B. G. Marsden, *Annu. Rev. Astron. Astrophys.* **43**, 75 (2005).
3. Z. Sekanina, P. W. Chodas, *Astrophys. J.* **757**, 127 (2012).
4. C. J. Schrijver *et al*., *Science* **335**, 324 (2012).
5. M. J. Aschwanden *et al*., *Astrophys. J.* **756**, 124 (2012).
6. R. A. Frazin, A. M. Vásquez, F. Kamalabadi, *Astrophys. J.* **701**, 547 (2009).
7. P. Bryans, W. D. Pesnell, *Astrophys. J.* **760**, 18 (2012).
8. See supplementary text S1 for details on the relevant time scales.
9. See supplementary materials and methods.
10. See supplementary text S2 and movies S5 to S8.
11. K. H. Schatten, J. M. Wilcox, N. F. Ness, *Sol. Phys.* **6**, 442 (1969).
12. P. Riley *et al*., *Astrophys. J.* **653**, 1510 (2006).
13. $\tau_{OV,OVI}$ is calculated using the sum of the inverse of the electron impact ionization rates for $O^{4+} \rightarrow O^{5+}$ and $O^{5+} \rightarrow O^{6+}$ at $n_e = 1 \times 10^8$ cm^{-3} obtained from table 2 of (*7*).
14. Y.-D. Jia, M. R. Combi, K. C. Hansen, T. I. Gombosi, *J. Geophys. Res.* **112**, A05223 (2007).
15. Z. Sekanina, P. W. Chodas, *Astrophys. J.* **663**, 657 (2007).
16. O. Burhonov *et al*., *Minor Planet Electronic Circulars 2012-S63* (2012).

Acknowledgments: Supported by NASA SDO/AIA contracts. All observational data are freely available from the NASA/SDO, AIA, HMI, STEREO, and SECCHI science teams. Simulations were conducted using the NASA Pleiades and NSF Ranger supercomputers.

Supplementary Materials

www.sciencemag.org/cgi/content/full/340/6137/1196/DC1
Materials and Methods
Supplementary Texts S1 and S2
Figs. S1 to S4
Movies S1 to S8
References (*17*–*44*)

14 February 2013; accepted 24 April 2013
10.1126/science.1236550

A Major Asymmetric Dust Trap in a Transition Disk

Nienke van der Marel,[1]* Ewine F. van Dishoeck,[1,2] Simon Bruderer,[2] Til Birnstiel,[3] Paola Pinilla,[4] Cornelis P. Dullemond,[4] Tim A. van Kempen,[1,5] Markus Schmalzl,[1] Joanna M. Brown,[3] Gregory J. Herczeg,[6] Geoffrey S. Mathews,[1] Vincent Geers[7]

The statistics of discovered exoplanets suggest that planets form efficiently. However, there are fundamental unsolved problems, such as excessive inward drift of particles in protoplanetary disks during planet formation. Recent theories invoke dust traps to overcome this problem. We report the detection of a dust trap in the disk around the star Oph IRS 48 using observations from the Atacama Large Millimeter/submillimeter Array (ALMA). The 0.44-millimeter–wavelength continuum map shows high-contrast crescent-shaped emission on one side of the star, originating from millimeter-sized grains, whereas both the mid-infrared image (micrometer-sized dust) and the gas traced by the carbon monoxide 6-5 rotational line suggest rings centered on the star. The difference in distribution of big grains versus small grains/gas can be modeled with a vortex-shaped dust trap triggered by a companion.

Although the ubiquity of planets is confirmed almost daily by detections of new exoplanets (*1*), the exact formation mechanism of planetary systems in disks of gas and dust around young stars remains a long-standing problem in astrophysics (*2*). In